# Understanding Polymorph Transformations in Core-Chlorinated Naphthalene Diimides and their Impact on Thin-Film Transistor Performance

*Geoffrey E. Purdum, Nan Yao, Arthur Woll, Thomas Gessner, Ralf Thomas Weitz, and Yueh-Lin Loo**

**Though charge transport is sensitive to subtle changes in the packing motifs of molecular semiconductors, research addressing how intermolecular packing influences electrical properties has largely been carried out on single-crystals, as opposed to the more technologically relevant thin-film transistors (TFTs). Here, independent and reversible access to the monoclinic and triclinic crystal structures of a core-chlorinated naphthalene tetracarboxylic diimide (NTCDI-1) is demonstrated in polycrystalline thin films via post-deposition annealing. Time-resolved measurements of these transitions via UV–visible spectroscopy and grazing-incidence X-ray diffraction indicate that the polymorphic transformations follow second-order Avrami kinetics, suggestive of 2D growth after initial nucleation. Thin-film transistors comprising triclinic NTCDI-1 consistently outperform those comprising its monoclinic counterpart. This behavior contrasts that of single-crystal transistors in which devices comprising monoclinic crystals are consistently superior to devices with triclinic crystals. This difference is attributed to more uniform in-plane charge transport in polycrystalline thin films having the triclinic compared to the monoclinic polymorph. As the mobility of TFTs is a reflection of ensemble-average charge transport across crystalline grains having different molecular orientations, this study suggests that among different polymorphs of a particular molecular semiconductor, those with smaller in-plane anisotropy are more beneficial for efficient lateral charge transport in polycrystalline devices.**

## 1. Introduction

Charge transport in molecular semiconductors is generally thermally activated as charges hop from one molecule to its neighboring molecule through $\pi$-orbital overlap. Subtle changes in the intermolecular packing in crystalline molecular semiconductors can therefore drastically impact intermolecular electronic coupling and substantially influence charge transport.[1,2] It is thus not surprising that molecular semiconductors having polymorphic crystal structures,[3–9] each having distinct intermolecular packing, exhibit differences in the efficacy of charge transport. Yet, assessing which polymorphic crystal structure is most efficient for charge transport is complicated by the fact that even within a single polymorph, charge transport anisotropy exists along different crystallographic directions due to the directionality of $\pi$-orbital overlap. This charge transport anisotropy, for example, results in a threefold to fourfold difference in mobility of field-effect transistors comprising rubrene and pentacene single crystals when measured along different crystallographic directions.[10,11]

In light of this complication, the elucidation of charge transport efficacy between polymorphs has largely been limited to comparisons of transistor mobilities in which polymorphic single crystals are specifically oriented with $\pi$-stacking in the direction of intended charge transport. In this context, single-crystal transistors of orthorhombic rubrene exhibit device mobilities that are an order of magnitude higher along [010] than those of triclinic rubrene along [100].[6,12] Devices comprising $\beta$-crystals of dihexyl-substituted dibenzo[d,d′[thieno[3,2-b;4,5-b′]dithiophenes, C6-DBTBT, exhibit mobilities that are twice as high as those comprising

G. E. Purdum, Prof. Y.-L. Loo
Department of Chemical and Biological Engineering
Princeton University
Princeton, NJ 08544, USA
E-mail: lloo@princeton.edu
Dr. N. Yao
Princeton Institute for Science and Technology of Materials
Princeton University
Princeton, NJ 08544, USA
Dr. A. Woll
Cornell High Energy Synchrotron Source
Cornell University
Ithaca, NY 14853, USA
Dr. T. Gessner
BASF SE
GMO/O, A30, 67056 Ludwigshafen, Germany
Dr. R. T. Weitz
BASF SE
GMO/F-J542s, 67056 Ludwigshafen, Germany

DOI: 10.1002/adfm.201502412


© 2015 WILEY-VCH Verlag GmbH & Co. KGaA, Weinheim

its $\alpha$-crystals, with this difference in mobility attributed to a decrease in the effective mass along the *b*-axis of the $\beta$-crystals compared to the *a*-axis of the $\alpha$-crystals.[13] These changes in intermolecular packing between different polymorphic crystal structures need not be big, as shown in devices comprising single crystals of difluorinated triethylsilylethynyl anthradithiophene, diF TES ADT, in which a mere 1%–2% difference in unit cell dimensions between the low- and high-temperature polymorphs resulted in a threefold difference in charge transport activation energy.[14]

While these single-crystal studies clearly show how polymorphism can impact electrical properties, they do not directly translate to the technologically more relevant platform of polycrystalline thin-film devices, in which charge carriers sample many crystallographic directions as they travel from the source to the drain electrodes. Yet, with the exception of a few recent studies,[15,16] the influence of polymorphism on thin-film electrical properties is rarely addressed, in large part because of the difficulty in producing polymorphically distinct thin films in a controlled manner. Most polymorphs are discovered as single crystals under very specific and stringent growth conditions. Exceptions to this generalization are metastable thin-film polymorphs that only exist when the growth of molecular semiconductor domains are restricted in one dimension.[16,17] Depending on the choice of substrate, film thickness and substrate temperature during growth, for example, pentacene can adopt several thin-film polymorphs that upon post-deposition processing convert irreversibly back to its thermodynamically more favored bulk polymorphs.[18–21] Solvent-vapor annealing has also been shown to convert contorted-hexabenzocoronene (c-HBC) thin films having the $P2_1/c$ polymorph into a second polymorph—likely triclinic—whose lattice dimensions and intermolecular packing have yet to be identified.[15] These findings suggest that post-deposition processing can transform the crystalline structure of thin films from one polymorph to another, albeit under very specific processing conditions.

Here, we describe an investigation of the polymorphic structures of a core-chlorinated naphthalene diimide, NTCDI-1, whose chemical structure is shown in **Figure 1**a, in polycrystalline thin films. We report the first access of NTCDI-1's monoclinic polymorph in thin films, and its reversible transformation to the more commonly accessed triclinic polymorph. Unlike many other molecular semiconductors exhibiting metastable thin-film polymorphs, the reversible transformation between NTCDI-1's two distinct polymorphs has enabled us to quantify the kinetics and elucidate the mechanism of this polymorphic transformation. Previous work on nonchlorinated naphthalene diimides has been focused on their use as electron transporting organic semiconductors resulting in device mobilities ranging from $10^{-1}$ to $10^{-3}$ $cm^2$ $V^{-1}$ $s^{-1}$.[22–25] Thermally evaporated and solution-sheared thin films of NTCDI-1 readily adopt its triclinic polymorph; thin-film transistors comprising triclinic NTCDI-1 exhibit mobilities as high as 1.3 $cm^2$ $V^{-1}$ $s^{-1}$.[26–29] Single-crystal transistors comprising triclinic NTCDI-1 exhibit a maximum mobility of 3.5 $cm^2$ $V^{-1}$ $s^{-1}$, while single-crystal transistors comprising its monoclinic polymorph exhibit mobilities as high as 8.6 $cm^2$ $V^{-1}$ $s^{-1}$ along its *c*-axis.[30,31] With access to the monoclinic polymorph of NTCDI-1 in polycrystalline thin films, we have fabricated and measured thin-film transistors having this polymorph and found its mobility to be consistently lower than those of thin-film transistors having the triclinic polymorph. That charge transport is more efficient in the triclinic polymorph compared to the monoclinic polymorph in thin-film transistors but not in single-crystal devices stems from the broad distribution of in-plane molecular orientations that is sampled in polycrystalline films. In the case of NTCDI-1, the mobilities of thin-film transistors appear to be dominated by charge transport anisotropy along different in-plane molecular orientations, as opposed to the specific polymorph itself.

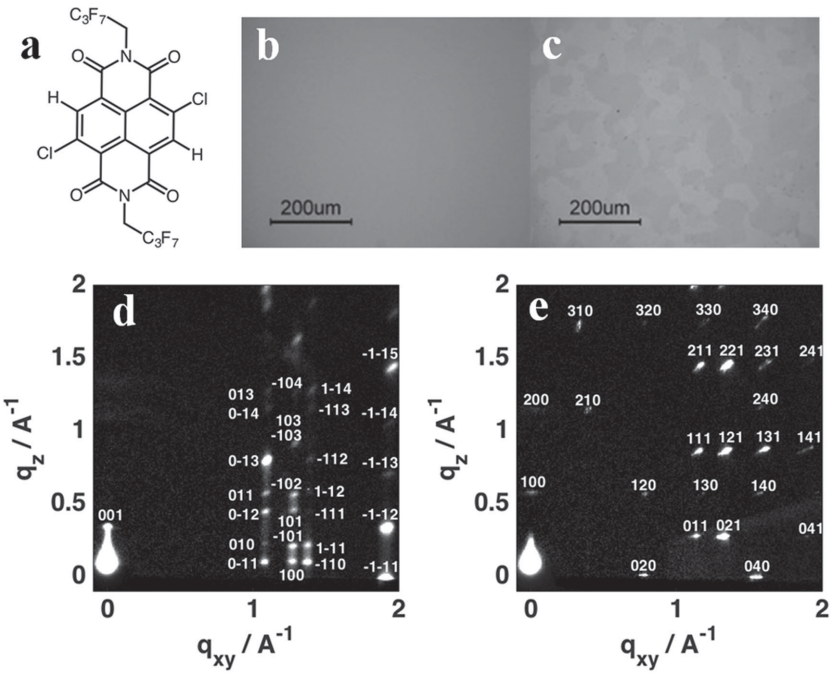


**Figure 1.** a) Chemical structure of NTDCI-1. b,c) Optical images of an as-evaporated and acetone-vapor annealed NTCDI-1 thin film, respectively. d,e) GIXD patterns of the films shown in (b) and (c), respectively. The as-evaporated film adopts a triclinic crystal structure, while the acetone-vapor annealed film adopts a monoclinic crystal structure. Reflections have been indexed per single-crystal crystallographic data.

## 2. Results and Discussion

### 2.1. Thin-Film Structure

Figure 1b shows an optical image of an 80 nm thick NTCDI-1 thin film on an *n*-octadecyltrichlorosilane (OTS)-treated silicon wafer with a 300 nm thick thermally grown oxide layer. This film is optically featureless. Exposing the thin film to acetone


© 2015 WILEY-VCH Verlag GmbH & Co. KGaA, Weinheim

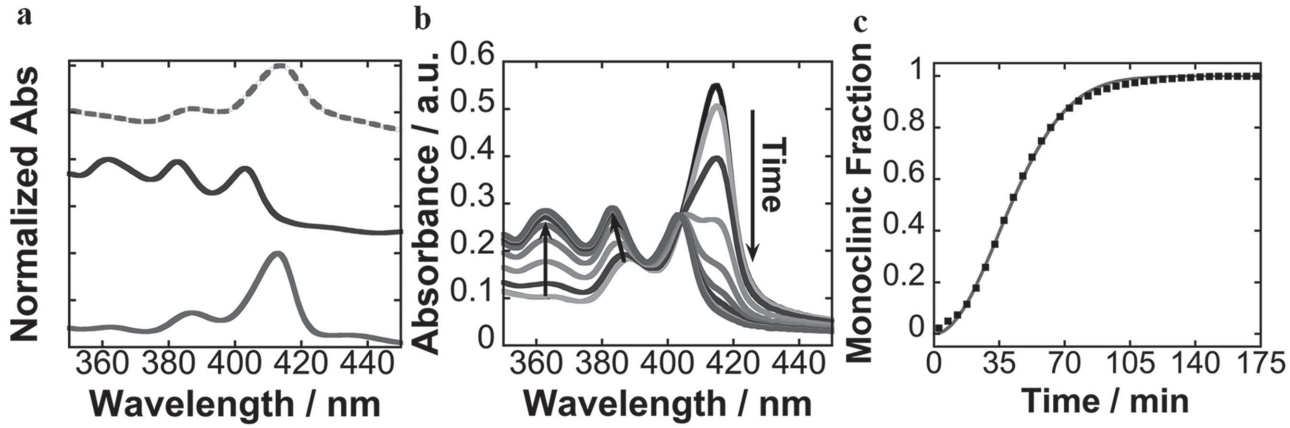


**Figure 2.** a) Normalized UV–vis absorbance spectra of the as-evaporated (bottom trace, solid), acetone-vapor annealed (middle trace, solid), and acetone-vapor annealed plus thermally annealed (top trace, dashed) films illustrating the reversible transformation between the two polymorphs. b) In situ UV–vis absorbance spectra during acetone-vapor annealing of a triclinic film. c) Fractional conversion of the triclinic polymorph to the monoclinic polymorph. The actual data points are represented by squares while the solid curve represents the best-fit to the second-order Avrami equation.

vapors in a closed Petri dish results in structural transformation; large domains on the order of a hundred micrometers appear throughout the film, as seen in Figure 1c. We conducted grazing-incidence X-ray diffraction (GIXD) measurements to elucidate the morphologies of NTCDI-1 thin films before and after post-deposition solvent-vapor annealing. Figure 1d,e shows the 2D GIXD patterns associated with the as-evaporated and acetone-vapor annealed films, respectively. We have been able to index the X-ray diffraction patterns according to the published crystal structures of NTCDI-1;[30] the Miller indices of the reflections are provided for clarity in Figure 1d,e. Upon deposition, NTCDI-1 is highly crystalline and adopts its triclinic crystal structure. NTCDI-1 is also preferentially oriented out-of-plane, with the (001) plane of its triclinic unit cell parallel to the substrate, as evidenced by the sharp reflection at $q_z$ = 0.34 Å$^{-1}$ along $q_{xy} = 0$, corresponding to NTCDI-1 preferentially oriented edge-on on the substrate. Although NTCDI-1 is preferentially oriented out-of-plane, the film is polycrystalline, with an absence of any overall preferred in-plane orientation. The acetone-vapor annealed film shows a significantly different diffraction pattern. Here, the (001) reflection associated with the triclinic crystal structure is absent, replaced with a reflection at $q_z$ = 0.56 Å$^{-1}$ along $q_{xy} = 0$, which we have been able to match to the (100) reflection of its monoclinic polymorph. It thus appears that acetone-vapor annealing transforms the film from its triclinic structure to its monoclinic structure, with this being the first report of its access in thin films. The monoclinic crystals are preferentially oriented with their (100) planes parallel to the substrate, also corresponding to NTCDI-1 preferentially oriented edge-on on the substrate; the $\pi$-planes of NTCDI-1, however, are tilted 49° away from the substrate normal. The film remains polycrystalline, with no preferential in-plane orientation after acetone-vapor annealing. That we are able to induce the triclinic to monoclinic polymorph transformation in NTCDI-1 thin films with solvent-vapor annealing appears to be generalizable; Figure S1 (Supporting Information) demonstrates that the monoclinic polymorph of NTCDI-1 is accessible with a wide range of solvents.

### 2.2. Polymorphic Transformations

**Figure 2**a shows normalized UV–visible (UV–vis) absorbance spectra for an as-evaporated NTCDI-1 thin film, an acetone-vapor annealed film, and a film that was acetone-vapor annealed and then isothermally annealed at 175 °C for 5 min. The UV–vis spectrum of the as-evaporated film exhibiting the triclinic polymorph displays a peak absorbance at 414 nm and a shoulder at 388 nm. Upon transforming to the monoclinic polymorph after exposure to acetone vapor, the UV–vis spectrum exhibits a blue shift, with its peak absorbance now located at 404 nm. The UV–vis spectrum of the monoclinic polymorph also reveals two additional absorbances at 384 and 364 nm. The UV–vis absorbance spectra of NTCDI-1 thin films are consistent with those of single crystals; the monoclinic polymorph exhibits H-type coupling, which is manifested by a blue shift in its absorbance spectrum relative to that of the triclinic polymorph, which exhibits J-type coupling.[30] To test whether the polymorphic transformation is reversible, we subjected acetone-vapor annealed films to isothermal annealing, as the transformation from monoclinic to triclinic polymorphs in single crystals was reported to occur at 180 °C.[30] Annealing the acetone-vapor annealed films at elevated temperatures, however, results in concurrent sublimation of NTCDI-1, making measurements difficult. To limit sublimation, we deposited a 2 µm thick layer of Cytop atop the acetone-vapor annealed films prior to thermal annealing. The UV–vis spectrum of the acetone-vapor annealed film after isothermal annealing at 175 °C for 5 min resembles that of the as-evaporated thin film, confirming its transformation from the monoclinic polymorph back to the triclinic polymorph. The polymorphic transformation in NTCDI-1 thus appears reversible, suggesting that the triclinic polymorph is thermodynamically stable at high temperatures, but metastable at room temperature.

To quantify the kinetics of transformation from the triclinic to monoclinic polymorphs, we performed in situ UV–vis absorbance spectroscopy during solvent-vapor annealing. Due to differences in the absorbance spectra of the triclinic


© 2015 WILEY-VCH Verlag GmbH & Co. KGaA, Weinheim

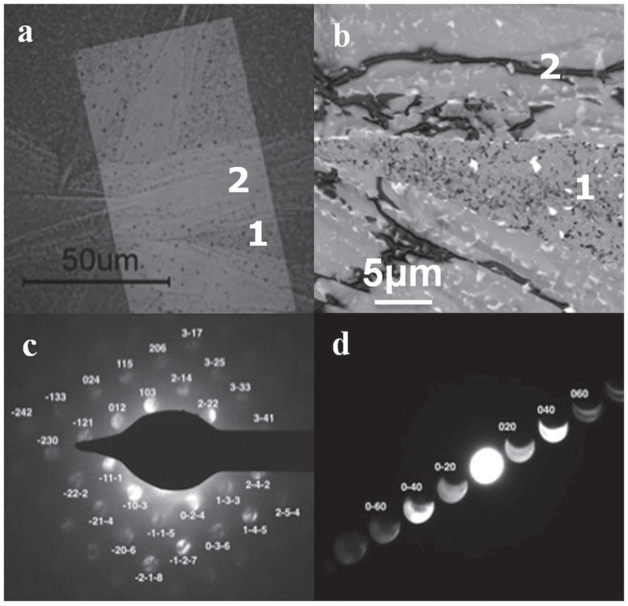


**Figure 3.** a) Optical image of an NTCDI-1 thin film exposed to acetone vapors for 45 min. b) Bright-field transmission electron micrograph of the same film. The portion of the film that has not yet transformed from the triclinic to monoclinic polymorph is labeled "1," whereas the region that has transformed to the monoclinic polymorph is labeled "2." Selected-area electron diffraction patterns obtained from c) region 1 with its reflections indexed according to the triclinic crystal structure, and d) region 2 with its reflections indexed according to the monoclinic crystal structure.

and monoclinic polymorphs, one can track the polymorphic transformation by fitting each of the absorbance spectra to a linear superposition of the absorbance spectrum of each polymorph. Figure 2b shows the time evolution of the UV–vis absorbance spectra of NTCDI-1 during solvent-vapor annealing with acetone. The peak at 414 nm, associated with the triclinic polymorph, monotonically decreases, while the absorbance at 404, 384, and 364 nm, all associated with the monoclinic polymorph, increases. Figure 2c tracks the fractional conversion of the triclinic to monoclinic polymorph. The transformation follows second-order Avrami kinetics, with a half-time of $48 \pm 6$ min. That the kinetics of transformation is second-order ($n = 2$) is consistent with 2D growth of monoclinic domains initiated by existing nuclei during solvent-vapor annealing; further consistent with this assertion, we do not observe subsequent formation of additional nuclei on extended solvent-vapor annealing.[32] To investigate the morphological changes during solvent-vapor annealing, we used selected-area electron diffraction (SAED) to examine a film that had been arrested during the triclinic to monoclinic transformation. **Figure 3**a shows an optical image of this film and Figure 3b shows the corresponding bright-field transmission electron micrograph of the film. Here, we observe two distinct regions; the region labeled 1 consists of speckles whereas the region labeled 2 consists of macroscopic ribbon-like structures; these ribbon structures can also be seen in portions of Figure 3a. Figure 3c,d shows the SAED from regions 1 and 2, respectively, which were obtained using a spot size of 1–2 nm. Based on the indexing of reflections in the SAED patterns, region 1 corresponds to the triclinic structure and region 2 adopts the monoclinic structure. Our SAED analysis indicates that both regions remain highly-crystalline, as evidenced by the single-crystal-like diffraction patterns that were obtained in each region separated by only a few micrometers. We thus surmise that the polymorphic transformation must only occur locally—as opposed to globally—at the growth front of these macroscopic ribbon structures.

To probe the reverse transformation from the monoclinic polymorph back to triclinic, we employed in situ GIXD during thermal annealing of a solvent-vapor annealed film at 175 °C. **Figure 4**a shows the time evolution of the GIXD patterns. We observed a monotonic decrease in the intensity of the monoclinic reflections with a concomitant emergence of the triclinic reflections as isothermal annealing progresses, indicative of the polymorphic transformation from monoclinic to triclinic. Figure 4b tracks the integrated intensities of the (100) and (–101) reflections associated with the triclinic polymorph at $q_{xy} = 1.26$ Å$^{-1}$ and $q_z = 0.13$ Å$^{-1}$, and that at $q_z = 0.18$ Å$^{-1}$, respectively, as well as the (021), (121), and (131) reflections associated with the monoclinic polymorph along $q_{xy} = 1.29$ Å$^{-1}$ at $q_z = 0.27$ Å$^{-1}$ and $q_z = 0.84$ Å$^{-1}$ and at $q_{xy} = 1.54$ Å$^{-1}$ and $q_z = 0.84$ Å$^{-1}$, respectively, to quantify the kinetics of transformation. The intensity

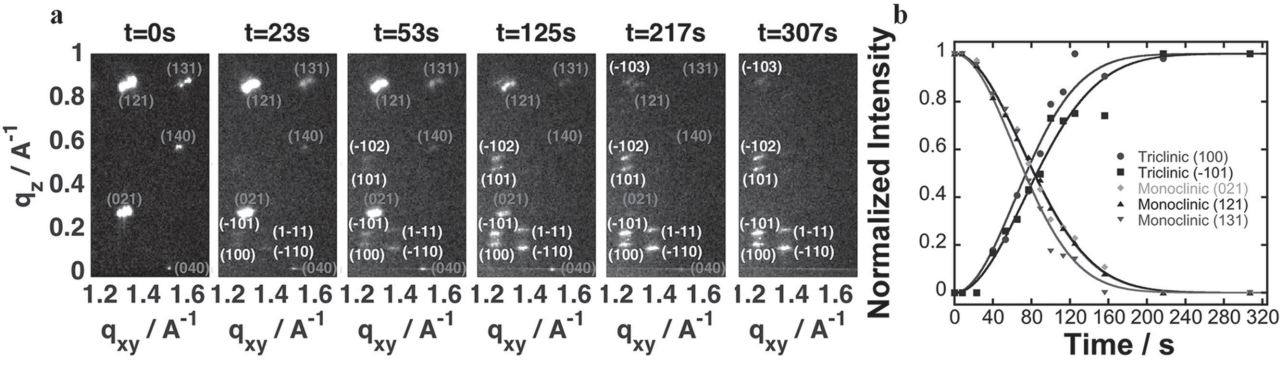


**Figure 4.** a) GIXD patterns of a film comprising the monoclinic polymorph isothermally annealed at 175 °C at various time points. The film converts from its monoclinic polymorph to its triclinic polymorph, as evidenced by the progressive decrease in intensity of the monoclinic reflections (labeled in gray) and the concomitant growing intensity of the triclinic reflections (labeled in white). b) The normalized intensities of the triclinic (100) and (–101) and monoclinic (021), (121), and (131) reflections are shown as a function of time. The solid lines are fits of the second-order Avrami equation to the data.


© 2015 WILEY-VCH Verlag GmbH & Co. KGaA, Weinheim

evolution associated with each reflection is best described by second-order Avrami kinetics, yielding an internally consistent half-time of 80 ± 5 s. This half-time is an order of magnitude smaller than that associated with the reverse transformation. Given that the kinetics of transformation is highly dependent on the conditions employed to induce transformation, we speculate that the kinetics to transform to the monoclinic polymorph is substantially slower because, under the conditions we employed, acetone vapors must penetrate and plasticize NTCDI-1 before any rearrangement can take place. Interestingly, the X-ray reflections associated with the monoclinic polymorph remain sharp throughout the isothermal transformation, suggesting that the distribution of molecular orientations does not change substantially during transformation. Consistent with our SAED data, we thus surmise that the transformation is not driven by global disordering of the monoclinic polymorph before the triclinic polymorph sets in; instead, the transformation must take place locally. It is also worth noting that the kinetics of transformation, as probed by the emergence and disappearance of the out-of-plane (001) reflection at $q_z$ = 0.34 Å$^{-1}$ associated with the triclinic and the (100) reflection at $q_z$ = 0.56 Å$^{-1}$ associated with the monoclinic polymorphs, respectively, shown in Figure S2 (Supporting Information), is faster than that probed by quantifying the intensity evolution of the in-plane reflections shown in Figure 4. While the intensity evolution associated with the out-of-plane reflections is still best described by second-order Avrami kinetics, the extracted half-time associated with the monoclinic-to-triclinic transformation is 55 ± 5 s instead of 80 ± 5 s. Our data thus indicate that the kinetics to transform from the monoclinic to the triclinic polymorph is faster in the out-of-plane direction compared to the in-plane direction. Detailed molecular modeling is currently underway to shed light on this peculiarity during its polymorphic transformation.

### 2.3. Device Performance

With an understanding of how to access both monoclinic and triclinic polymorphs in thin films, bottom-gate, top-contact field-effect transistors were fabricated to test the electrical properties of each in thin films. Active layers comprising the triclinic polymorph were prepared by depositing NTCDI-1 on an OTS-treated $Si/SiO_2$ dielectric surface, while the monoclinic polymorph was accessed by acetone-vapor annealing a thermally evaporated NTCDI-1 film. The morphologies of these films are similar to those shown in Figure 1b,c. **Figure 5** shows the transfer characteristics, taken in the saturation regime at $V_{SD}$ = 70 V, for representative devices comprising NTCDI-1 in its triclinic and monoclinic polymorphs in the active channels. The average and standard deviation of device parameters extracted from 50 devices are shown in **Table 1**. While the on/off ratio is comparable at $10^6$–$10^8$ between the two sets of devices, the threshold voltage and mobility are dramatically different. More specifically, the threshold voltage increases from –0.5 ± 2.8 V to 21.0 ± 10.0 V

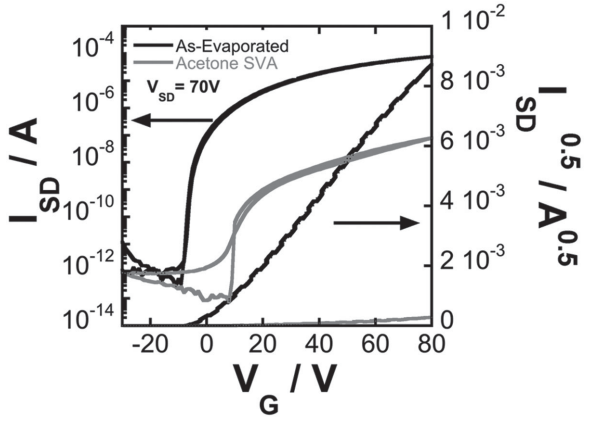


**Figure 5.** Transfer characteristics of thin-film transistors incorporating as-evaporated and acetone-vapor annealed films as active layers. Devices with as-evaporated active layers consistently outperform those with polycrystalline solvent-vapor annealed active layers.

in devices comprising the triclinic active channels compared to those having the monoclinic active channels. We believe this difference in threshold voltage stems from the presence of additional traps at the organic semiconductor-dielectric interface in devices containing the monoclinic polymorph as solvent-vapor annealing introduces solvent molecules that are subsequently trapped at that charge transport interface. Such dramatic threshold voltage shifts have previously been observed in 1,2-dichloroethane-vapor annealed thin-film transistors of triethylsilylethynyl anthradithiophene, TES ADT.[33] Indeed, tracking the threshold voltage of devices having the monoclinic polymorph as a function of the choice of solvent employed during solvent-vapor annealing reveals the threshold voltage to be strongly correlated with solvent polarity. The mobility of the devices comprised of the triclinic polymorph at 0.69 ± 0.12 cm$^2$ V$^{-1}$ s$^{-1}$ is two orders of magnitude higher than those of devices comprising the monoclinic polymorph. We were initially surprised by this finding given that single-crystal transistors of monoclinic NTCDI-1 exhibit a mobility that is almost three times higher than that of single-crystal transistors of triclinic NTCDI-1.[30] We now believe this discrepancy between mobilities extracted in thin-film and single-crystal transistors to stem from the polycrystalline nature of active channels in thin-film transistors.

Our GIXD and SAED experiments have informed us that NTCDI-1 thin films of both polymorphs exhibit strong preferential out-of-plane orientation. In particular, the monoclinic

**Table 1.** Summary of device characteristics of thin-film transistors comprising the triclinic and monoclinic polymorphs of NTCDI-1.

| Sample | Polymorph | $\mu$[a)] [cm$^2$ V$^{-1}$ s$^{-1}$] | $V_T$ [V] | On/Off ratio |
|---|---|---|---|---|
| As-evaporated[b)] | Triclinic | 0.69 ± 0.12 (0.96) | –0.5 ± 2.8 | $10^7$–$10^8$ |
| Acetone-vapor annealed[b)] | Monoclinic | 0.0032 ± 0.0020 (0.013) | 21.0 ± 10.0 | $10^5$–$10^6$ |
| Toluene-vapor annealed needles[c)] | Monoclinic | 1.20 ± 0.68 (2.32) | 0.7 ± 4.7 | $10^5$ |

[a)]Values reported in parenthesis represent maximum mobility; [b)]Device statistics, reported as average ± standard deviation, were obtained from over 50 devices; [c)]Device statistics were obtained from 14 devices.


© 2015 WILEY-VCH Verlag GmbH & Co. KGaA, Weinheim

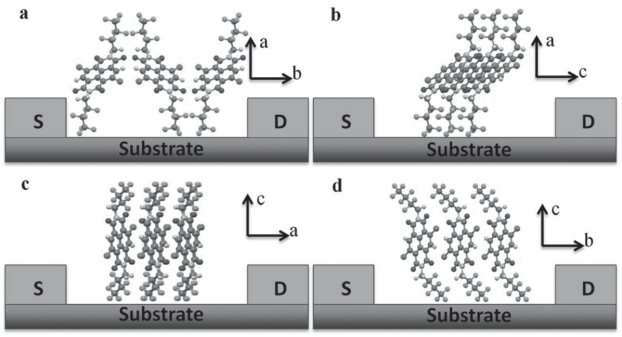


**Figure 6.** Illustrations of possible molecular orientations of NTCDI-1 within the active channel of a thin-film transistor. The monoclinic polymorph is oriented with the *a*-axis out-of-plane, limiting the in-plane crystallographic directions to those illustrated in (a) and (b) and other in-plane orientations between the two. The triclinic polymorph is oriented with the *c*-axis out-of-plane, thus the in-plane orientations that can be sampled in the active channel range between those shown in (c) and (d).

polymorph is oriented with its *a*-axis along the substrate normal, while the triclinic polymorph is oriented with its *c*-axis along the substrate normal. But the crystalline grains of neither polymorph exhibit any preferential in-plane orientation. Given that the grain sizes are much smaller than the channel length of our thin-film transistors, charges will have to traverse multiple crystalline grains having in-plane orientations that are different from each other in order to be collected at the drain electrodes. **Figure 6**a,b shows illustrations of the monoclinic polymorph with its *b*- and *c*-axes preferentially oriented between the source and drain electrodes, respectively. Given that the *a*-axis is preferentially oriented out-of-plane, these two orientations flank the range of all possible in-plane orientations that monoclinic grains of NTCDI-1 can adopt. Given the extensive $\pi$-stacking along the *c*-axis, it is easy to picture how charges can traverse from the source to the drain electrodes when monoclinic grains of NTCDI-1 adopt the orientation depicted in Figure 6b. It must, however, be difficult for charges to transport across monoclinic grains of NTCDI-1 when they adopt the orientation depicted in Figure 6a, in which $\pi$-stacking from the source to drain electrodes is minimal. It thus appears that only when the *c*-axis is preferentially aligned along the intended charge transport direction can charges efficiently transport from the source and drain electrodes. Yet, the polycrystalline nature of NTCDI-1 active channels means that the in-plane orientations depicted in Figure 6a,b, as well as those in between, are sampled. It follows that the mobility measured in transistors comprising these polycrystalline thin-film active channels must reflect an ensemble-average quantity based on charge transport along these different crystallographic directions. Figure 6c,d shows illustrations of the triclinic polymorph with its *a*- and *b*-axes preferentially oriented between the source and drain electrodes, respectively. Again, since the triclinic polymorph is oriented with its *c*-axis out-of-plane, these two orientations are the extremes of the range of all possible in-plane orientations that NTCDI-1 can adopt. Given strong $\pi$-stacking along both the *a*- and *b*-axes, it is easy to envision charges traveling from the source to drain electrode in both cases. Since both of these orientations, along with others in between, are sampled in active channels of devices consisting of polycrystalline films, the enhanced mobility we measure with devices having the triclinic polymorph compared with those having the monoclinic polymorph as the active layer must stem from more isotropic in-plane charge transport in the triclinic polymorph. Despite the fact that charge transport along the $\pi$-stacking direction is more efficient in the monoclinic polymorph of NTCDI-1, our experiments point out the significance of charge transport anisotropy along different crystallographic directions in influencing the performance of thin-film devices. Not coincidentally, NTCDI-1 adopts a 2D brickwork-type packing motif in its triclinic polymorph, which has been proposed to be more efficient for lateral charge transport in thin-film devices compared to polymorphs that adopt a 1D packing motif,[34] like the one adopted by the monoclinic polymorph.

To further test this hypothesis, high aspect ratio monoclinic grains were accessed through concentrated solvent-vapor annealing of NTCDI-1 thin films having the triclinic polymorph. To access these needles, the bottom of the Petri dish was flooded with solvent, giving rise to a higher vapor concentration. While these needles are randomly oriented with respect to one another, top-contacts were positioned such that individual needles span the source and drain electrodes. From previous studies, it is known that the monoclinic polymorph forms needles with the long axis corresponding to the *c*-axis, or the $\pi$-stacking direction.[27,31] An optical image of a typical device comprising needles having the monoclinic polymorph developed in the presence of toluene vapors is shown in **Figure 7**a. Representative transfer characteristics for these devices are shown in Figure 7b. The electron mobilities, extracted from the saturation regime at $V_{SD}$ = 70 V, exceed 1 cm$^2$ V$^{-1}$ s$^{-1}$, with a maximum mobility of 2.3 cm$^2$ V$^{-1}$ s$^{-1}$, which is almost three orders of magnitude higher than polycrystalline thin-film devices comprising the same polymorph, and three to four times higher than those of thin-film devices comprising the triclinic polymorph. To confirm that transport in our devices takes place along the needles, Figure S3 (Supporting Information) shows device characteristics of the same transistor before and after a scratch is put through the needle. The substantial current drop after the needle had been damaged is a strong indication that transport had occurred predominately through the needle and not through the surrounding film that was present in the active channel. That we are able to recover the mobility of devices having the monoclinic polymorph in our control experiment reaffirms the importance

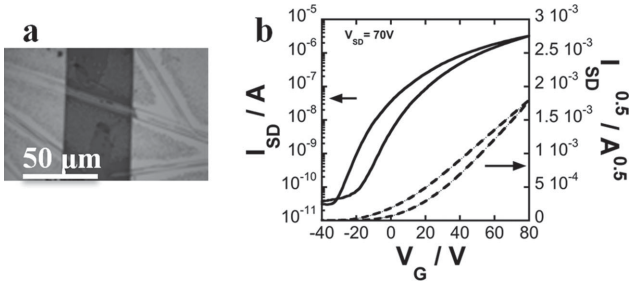


**Figure 7.** a) Optical image of monoclinic needles grown from toluene-vapor annealing. The average width of the needles was 4.9 ± 0.9 µm. b) Transfer characteristics of a representative OFET incorporating needles grown from toluene vapor.


© 2015 WILEY-VCH Verlag GmbH & Co. KGaA, Weinheim

of proper alignment of crystalline grains in addition to appropriate polymorph selection in influencing the electrical performance of devices. It is thus not surprising that polycrystalline thin-film transistors exhibit ensemble-average mobilities that reflect charge transport across a substantially broader distribution of in-plane molecular orientations.

## 3. Conclusion

We have demonstrated the ability to tune the molecular packing of NTCDI-1 in thin films through post-deposition processing. The triclinic polymorph is accessed upon thermal evaporation, while the monoclinic polymorph is accessed upon solvent-vapor annealing. Unique to NTCDI-1, both polymorphs are reversibly accessed. Field-effect transistors based on polycrystalline active channels of triclinic NTCDI-1 exhibit an electron mobility that is two orders of magnitude higher compared to devices having monoclinic NTCDI-1. While opposite of what one would have predicted based on the electrical characteristics of single-crystal devices, this discrepancy stems from the smaller charge transport anisotropy sampled by the distribution of in-plane molecular orientations in the triclinic polymorph as opposed to the monoclinic polymorph. Our experiments with thin-film devices thus indicate that while judicious selection of the polymorph is important for optimal device performance, possessing less in-plane anisotropy is far more critical than having a higher mobility along a specific crystallographic direction for polycrystalline thin-film devices.

## 4. Experimental Section

*Materials*: All solvents were purchased from Fisher Scientific and used as-received. *n*-octadecyltrichlorosilane (≥90%) was purchased from Sigma Aldrich and used as-received. The synthesis of NTCDI-1 followed reported procedures in the literature without further modifications.[27] Materials requests for NTCDI-1 should be directed to BASF SE.

*Substrate Preparation*: Si(100) wafers with thermally grown $SiO_2$ (300 nm thick; purchased from Process Specialties, Inc.) were used as gate and gate dielectric, respectively, for fabricating thin-film transistors. These same substrates were also used for GIXD measurements of NTCDI-1. The substrates were sonicated in deionized water, acetone, and isopropanol and dried with nitrogen. After cleaning, the substrates were exposed to oxygen plasma for 10 min. After plasma treatment, the substrates were placed in a $35 \times 10^{-3}$ M solution of *n*-octadecyltrichlorosilane in trichloroethylene. After 1 h, the substrates were removed from the solution and cleaned with toluene and chloroform.

*Thin-Film Deposition*: NTCDI-1 was thermally evaporated at a rate of 0.5–1 Å $s^{-1}$ under a base pressure of $1 \times 10^{-6}$ mbar atop OTS-treated $SiO_2$/Si substrates to form a uniform film with a thickness of 80 nm.

*Solvent-Vapor Annealing*: NTCDI-1 films were placed in a covered Petri dish (100 mm outside diameter) at room temperature in the presence of a solvent reservoir containing 10 mL of the solvent of choice. These films remained in the closed environment for solvent-vapor annealing; the exposure times varied depending on the solvent choice and its vapor pressure. During solvent-vapor annealing, NTCDI-1 thin films transformed from its triclinic polymorph to its monoclinic polymorph. This transformation took place over several hours when acetone was used, but over multiple days when chlorobenzene was the solvent instead.

*Structural Characterization*: GIXD experiments were conducted at the G1 station (9.95 ± 0.05 keV) of the Cornell High Energy Synchrotron Source. The beam was chosen to be 0.05 mm tall and 1 mm wide. The width of each sample was 5 mm. The X-ray beam was aligned above the film's critical angle but below that of the substrate, at a 0.18° incident angle with the substrate. X-ray scattering was collected with a 2D CCD detector, positioned 111.5 mm from the sample. All GIXD images have been background subtracted. For in situ GIXD experiments, the films were not coated with Cytop. UV–vis absorption was measured using an Agilent Technologies Cary 5000 spectrophotometer. Transmission electron microscopy (TEM) and SAED were performed on an FEI Titan$^3$ microscope using a bottom mounted FEI Ceta CMOS camera. The accelerating voltage was 200 kV. For SAED, the spot size was set to 1–2 nm. Films were deposited via thermal evaporation onto a silicon nitride TEM grid (SiMPore) and subsequently exposed to acetone vapors for 45 min to induce partial polymorphic transformation.

*Device Fabrication and Characterization*: Top-contact (Au), bottom-gate (Si) thin-film transistors with an OTS-treated 300 nm $SiO_2$ dielectric layer were fabricated with 80-nm thick NTCDI-1 films (same as in GIXD studies). After NTCDI-1 deposition and, in the case of devices having the monoclinic polymorph, subsequent solvent-vapor annealing, 60 nm of Au were thermally evaporated through a stencil mask to produce source and drain contacts. The channel length and width were 50 and 200 μm, respectively. Devices comprising high aspect ratio monoclinic grains had channel lengths of 50 μm and widths corresponding to the width of a grain, estimated to be 4.9 ± 0.9 μm. All transistors were tested in air using an Agilent 4155C semiconductor parameter analyzer. The electron mobilities were estimated in the saturation regime at $V_{SD} = 70$ V. Threshold voltages were calculated by extrapolating the zero point of the square root of current versus the gate voltage in the saturation regime. On/off current ratios were calculated by taking the ratio of $I_{SD}$ at 70 V (on) and at the turn-on voltage (off) from the transfer characteristics.

## Supporting Information

Supporting Information is available from the Wiley Online Library or from the author.

## Acknowledgements

Portion of this work was conducted at the Cornell High Energy Synchrotron Source (CHESS), which is supported by the National Science Foundation and the National Institutes of Health/National Institute of General Medical Sciences under NSF awards DMR-0936384 and DMR-1332208. G.E.P. acknowledges support from DoD, Air Force Office of Scientific Research, the National Defense Science and Engineering Graduate (NDSEG) Fellowship Program, 32 CFR 168a. This work was also partially supported by an NSF MRSEC grant through Princeton Center for Complex Materials (DMR-1420541).

Received: June 12, 2015
Revised: August 7, 2015
Published online: September 23, 2015

[1] J. L. Bredas, J. P. Calbert, D. A. da Silva Filho, J. Cornil, *Proc. Natl. Acad. Sci. USA* **2002**, *99*, 5804.
[2] M. Mas-Torrent, C. Rovira, *Chem. Rev.* **2011**, *111*, 4833.
[3] C. C. Mattheus, A. B. Dros, J. Baas, G. T. Oostergetel, A. Meetsma, J. L. de Boer, T. T. M. Palstra, *Synth. Met.* **2003**, *138*, 475.
[4] C. C. Mattheus, A. B. Dros, J. Baas, A. Meetsma, J. L. de Boer, T. T. M. Palstra, *Acta Crystallogr. Sect. C: Cryst. Struct. Commun.* **2001**, *57*, 939.


© 2015 WILEY-VCH Verlag GmbH & Co. KGaA, Weinheim

[5] L. W. Huang, Q. Liao, Q. Shi, H. B. Fu, J. S. Ma, J. N. Yao, *J. Mater. Chem.* **2010**, *20*, 159.
[6] T. Matsukawa, M. Yoshimura, M. Uchiyama, M. Yamagishi, A. Nakao, Y. Takahashi, J. Takeya, Y. Kitaoka, Y. Mori, T. Sasaki, *Jpn. J. Appl. Phys.* **2010**, *49*, 085502.
[7] S. Destri, M. Mascherpa, W. Porzio, *Adv. Mater.* **1993**, *5*, 43.
[8] R. A. Laudise, P. M. Bridenbaugh, T. Siegrist, R. M. Fleming, H. E. Katz, A. J. Lovinger, *J. Cryst. Growth* **1995**, *152*, 241.
[9] T. Siegrist, C. Kloc, R. A. Laudise, H. E. Katz, R. C. Haddon, *Adv. Mater.* **1998**, *10*, 379.
[10] V. C. Sundar, J. Zaumseil, V. Podzorov, E. Menard, R. L. Willet, T. Someya, M. E. Gershenson, J. A. Rogers, *Science* **2004**, *303*, 1644.
[11] J. Y. Lee, S. Roth, Y. W. Park, *Appl. Phys. Lett.* **2006**, *88*, 252106.
[12] T. Matsukawa, M. Yoshimura, K. Sasai, M. Uchiyama, M. Yamagishi, Y. Tominari, Y. Takahashi, J. Takeya, Y. Kitaoka, Y. Mori, T. Sasaki, *J. Cryst. Growth* **2010**, *312*, 310.
[13] P. He, Z. Tu, G. Zhao, Y. Zhen, H. Geng, Y. Yi, Z. Wang, H. Zhang, C. Xu, J. Liu, X. Lu, X. Fu, Q. Zhao, X. Zhang, D. Ji, L. Jiang, H. Dong, W. Hu, *Adv. Mater.* **2015**, *27*, 825.
[14] O. D. Jurchescu, D. A. Mourey, S. Subramanian, S. R. Parkin, B. M. Vogel, J. E. Anthony, T. N. Jackson, D. J. Gundlach. *Phys. Rev. B: Condes. Matter Mater. Phys.* **2009**, *80*, 085201.
[15] A. M. Hiszpanski, R. Baur, B. Kim, N. Tremblay, C. Nuckolls, A. Woll, Y.-L. Loo, *J. Am. Chem. Soc.* **2014**, *136*, 15749.
[16] Y. Diao, K. M. Lenn, W.-Y. Lee, M. A. Blood-Forsythe, J. Xu, Y. Mao, Y. Kim, J. A. Reinspach, S. Park, A. Aspuru-Guzik, G. Xue, P. Clancy, Z. Bao, S. C. B. Mannsfeld, *J. Am. Chem. Soc.* **2014**, *136*, 17046.
[17] Y. Diao, B. C. K. Tee, G. Giri, J. Xu, D. H. Kim, H. A. Becerril, R. M. Stoltenberg, T. H. Lee, G. Xue, S. C. B. Mannsfeld, Z. Bao, *Nat. Mater.* **2013**, *12*, 665.
[18] A. Brillante, I. Bilotti, R. Guido Della Valle, E. Venuti, A. Girlando, M. Masino, F. Liscio, S. Milita, C. Albonetti, P. D'angelo, A. Shehu, F. Biscarini,*Phys. Rev. B.* **2012**, *85*, 195308.
[19] M. Campione, S. Tavazzi, M. Moret, *J. Appl. Phys.* **2007**, *101*, 083512.
[20] D. J. Gundlach, T. N. Jackson, D. G. Schlom, S. F. Nelson, *Appl. Phys. Lett.* **1999**, *74*, 3302.
[21] A. Amassian, V. A. Pozdin, R. Li, D. M. Smilgies, G. G. Malliaras, *J. Mater. Chem.* **2010**, *20*, 2623.
[22] B. J. Jung, J. Sun, T. Lee, A. Sarjeant, H. E. Katz, *Chem. Mater.* **2009**, *21*, 94.
[23] Y. L. Lee, H. Hui-Lin, S. Y. Chen, T. R. Yew, *J. Phys. Chem. C.* **2008**, *112*, 1694.
[24] Th. B. Singh, S. Erten, S. Gunes, C. Zafer, G. Turkmen, B. Kuban, Y. Teoman, N. S. Sariciftci, S. Icli, *Org. Electron.* **2006**, *7*, 480.
[25] M. Ichikawa, Y. Yokota, H. G. Jeon, G. de Romeo Banoukepa, N. Hirata, N. Oguma, *Org. Electron.* **2013**, *14*, 516.
[26] M. Stolte, S. L. Suraru, F. Würthner, J. H. Oh, Z. Bao, J. Brill, M. Könemann, J. Qu, U. Zschieschang, H. Klauk, *Proc. SPIE* **2010**, *7778*, 777804.
[27] J. H. Oh, S. L. Suraru, W. Y. Lee, M. Könemann, H. W. Höffken, C. Röger, R. Schmidt, Y. Chung, W. C. Chen, F. Würthner, Z. Bao, *Adv. Funct. Mater.* **2010**, *20*, 2148.
[28] W. Y. Lee, J. H. Oh, S.-L. Suraru, W. C. Chen, F. Würthner, Z. Bao, *Adv. Funct. Mater.* **2011**, *21*, 4173.
[29] M. Stolte, M. Gsänger, R. Hofmockel, S.-L. Suraru, F. Würthner, *Phys. Chem. Chem. Phys.* **2012**, *14*, 14181.
[30] T. He, M. Stolte, C. Burschka, N. H. Hansen, T. Musiol, D. Kälblein, J. Pflaum, X. Tao, J. Brill, F. Würthner, *Nat. Commun.* **2015**, *6*, 5954.
[31] T. He, M. Stolte, F. Würthner, *Adv. Mater.* **2013**, *25*, 6951.
[32] S. S. Lee, S. Mauralidharan, A. R. Woll, M. A. Loth, Z. Li, J. E. Anthony, M. Haataja, Y.-L. Loo, *Chem. Mater.* **2012**, *24*, 2920.
[33] K. C. Dickey, J. E. Anthony, Y. L. Loo, *Adv. Mater.* **2006**, *18*, 1721.
[34] J. E. Anthony, S. Subramanian, S. R. Parkin, S. K. Park, T. N. Jackson, *J. Mater. Chem.* **2009**, *19*, 7984.


© 2015 WILEY-VCH Verlag GmbH & Co. KGaA, Weinheim